A LOCALLY CONSTRAINED STATISTICAL SHAPE MODEL FOR ROBUST NASAL CAVITY SEGMENTATION IN COMPUTED TOMOGRAPHY

Robin Huang[1], Ang Li[1], Lei Bi[1], Changyang Li[1], Paul Young[2], Gregory King[2], David Dagan Feng[1], and Jinman Kim[1]

[1]BMIT Research Group, School of Information Technologies, University of Sydney, Australia
[2]Woolcock Institute of Medical Research, University of Sydney, Australia

ABSTRACT

Accurate segmentation of the nasal cavity plays a pivotal role for the creation of patient specific nasal models which are essential for the diagnosis and treatment planning of nasal-related disorders and diseases, as well as for research on nasal drug delivery. However, the structure of the nasal cavity is difficult to segment due to the lack of boundary distinction to other connected airway components, such as the paranasal sinuses, which exhibits the same intensity range. Existing algorithms fail at differentiating the cavity from its surrounding structures. This paper presents a new method at segmenting the nasal cavity, designed to differentiate between the nasal and non-nasal airway. Our algorithm makes use of a range of statistical knowledge of the complex nasal anatomy through the introduction of a robust multi-atlas initialization for seeds derivation and the incorporation of a similarity guided statistical shape model (SSM). Our approach combines the shape variation energy of the SSM together with a modified locally constrained random walk algorithm to segment the nasal cavity. Our proposed algorithm was evaluated on 20 CT images and outperformed comparative state-of-the-art and conventional algorithms.

Index Terms— Segmentation, Nasal Cavity, CT

1. INTRODUCTION

The nasal cavity belongs to the upper respiratory tract and is a major passage for the transportation of oxygen into the lung. Accurate segmentation of the nasal cavity plays a pivotal role in the creation of patient specific nasal models for computational fluid dynamics which is essential for the treatment planning of nasal-related disorders and diseases [1, 2], be of benefit to endonasal surgeries [3], and is crucial for research on nasal airflow and drug delivery [4, 5]. Due to the complexity and diversity of the nasal structure as well as the lack of boundary distinction to other airway components, existing algorithms are unable to produce a standalone segmentation of the nasal cavity.

The current known methods [6-13] are capable of producing adequate segmentations of the upper respiratory tract consisting of the nasal cavity, paranasal sinuses and the pharynx using relatively simple algorithms such as thresholding [8-11], region growing [6, 7], level-sets [12], and level-sets distribution model [13]. However, the majority of them still requires manual delineation [6-9] and/or requires the imaging modality to be of cone-beam CT (CBCT) [9-12]. More importantly, these methods are restricted by their inability to differentiate and/or separate the nasal cavity from other airway regions components within the upper respiratory tract, thus limiting its application in nasal drug delivery [4] and computational fluid dynamics [14].

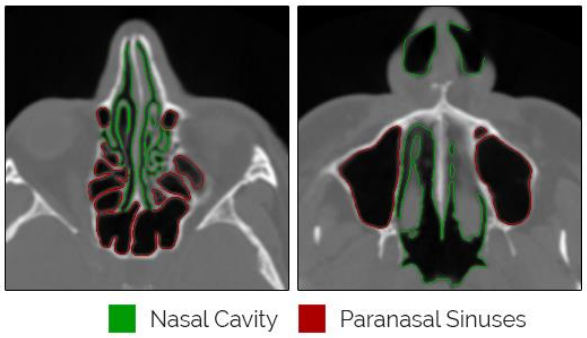

Figure 1. Examples illustrating the connectivity between the nasal cavity to other airway regions in CT.

The nasal cavity is recognized as a difficult structure to segment due to the complexity and diversity of its anatomy; its interconnectedness to other airway regions; the lack of clear boundaries; and the narrowness observed in many of its airway passages [2, 15]. Figure 1 exemplifies the close proximity of the paranasal sinuses to the nasal cavity and highlighted some of the connectivity observed between the two regions. In order to establish clear boundaries around the nasal cavity and to separate it from other airway regions, spatial and anatomical information needs to be utilized.

Statistical shape models (SSM) have been widely employed in medical image segmentation due to its ability at modelling the anatomy [16]. Based on a set of training data, the variability of a class of objects can be captured by means of a normal distribution, which can be used by the SSM for segmentation. However, due to the diversity of the nasal structure, it is challenging to establish precise point correspondence for the construction of a generic SSM.

Hence we turn our attention to SSM constructed via level-sets instead [17]. Level-set approaches do not require point correspondence, and recently they have been adapted to work with graph-based algorithms to overcome some of the known weakness in level-set segmentation [19]. Graph-based algorithms such as random walker (RW) [18] formulate an image as a graph, model voxels as graph vertices, assign weights to vertex connectivities and produce vertex labeling by minimizing energy functionals usually based on weights. Compared to other graph-based algorithms, RW can better localize specific regions within an image through the initialization of foreground and background voxels. This makes RW a preferable choice to be adapted with SSM shape priors for nasal segmentation.

In this study, we propose a new fully automated segmentation algorithm designed to overcome the challenges involved in differentiating the nasal cavity from other airway components of the same voxel intensity range. Compared to other literature, our paper makes the following contributions: (i) we combined RW with level-set shape priors and introduced it for nasal segmentation; and (ii) we present a novel constraint method to locally bind the estimated shape probabilities of RW at each differential iteration stage during segmentation to converge towards a global minimum. Our proposed method was evaluated with 20 volumes of clinical CT data.

2. METHODS AND MATERIAL

2.1 Materials and Ground Truth

Our dataset consisting of 20 head CT images was acquired from the department of Radiology at the Royal Prince Alfred hospital (Camperdown, NSW, Australia) taken via a GE Lightspeed-16 CT Scanner using Helical CT imaging protocols with an average exposure time of 707 seconds. The resulting images maintained a resolution of 220 by 220 mm (512×512 voxels) and a voxel depth of 1.25 mm. Our ground truth data was semi-automatically segmented using Geodesic Image Segmentation [20] by an experienced operator with the assistance of a nasal surgeon. The segmented data were further re-examined by a clinical doctor with expertise in CT-readings. The resulting ground truth segmentations were used in our algorithm as both training data for the level-set SSM and for the construction of the probabilistic atlas.

2.2 Methods

Initialization: Affine and Bspline registration using Elastix [21] is performed on the atlas CT images to align them to the input target image. The transformation parameters of the registration is then applied on the atlas segmentations to warp them to the same reference frame as the target image. A probabilistic multi-atlas A is constructed as the average of the registered segmentations $\{G_1, G_2, \dots, G_n\}$ over the total number of the atlases n, denoted as $A = \frac{1}{n}\sum_{j=1}^{n} G_j$.

Thresholding is applied on the input image to extract the position of the airway voxels. By overlaying A on top of the thresholded image T, an estimate P of the nasal cavity can be obtained from the union of the thresholded image and the atlas, defined as: $P = A \cup T$. The input image is further cropped in order to better localize the nasal cavity and to reduce the computation time. Smaller airway regions captured by P are removed to ensure accurate seeds derivation. Foreground seeds are derived from the remaining airway regions that lie within P. Background seeds are derived from tissue voxels and airway voxels of a distance σ away from P, with σ being a numerical parameter specified during initialization. Once the required seeds have been derived and an estimate of the nasal cavity P is obtained, we construct the shape priors to capture the statistical variances of the nasal cavity.

SSM Construction: We adopt a similar construction method as [17], where a mean offset matrix of the training data, denoted as $\{x_1 - \bar{x}, x_2 - \bar{x}, \dots, x_n - \bar{x}\}$ is constructed, with x_1 to x_n being the signed distance representations of the training shapes and $\bar{x}$ being the mean denoted as $\bar{x} = \frac{1}{n}\sum_{i=1}^{n} x_i$. The resulting eigenvector U and eigenvalues obtained from the singular value decomposition (SVD) of the mean offset matrix holds the decomposed features of the nasal cavity shape across a linear distribution. An estimate of a novel nasal shape s_{est}, can be represented by k principal components in a k-dimensional vector of coefficients, α: $S_{est} = U_k\alpha + \bar{x}$. Due to the diversity of the nasal cavity structure, it is necessary for outlier shapes to be removed from the training data. A similarity guided framework was implemented to assign a weight w to each training shape t calculated as $w = \frac{|P \cap t|}{|P| + |t| - |P \cap t|}$. Nasal shapes that scored below the mean weight were removed from the training dataset.

Segmentation: We embed the constructed SSM in a graph-based segmentation framework and formulate an image as a graph $G = (V, E)$, where each vertex $v \in V$ corresponds to an image voxel and each edge $e \in E$ connects two vertices in V. We borrow the idea from RW and construct the Dirichlet energy as $E_{rw} = z^T L z$, where L is the Laplacian matrix defined in [18] and denotes the pairwise affinities among the vertices in V, and $z \in R^{|V| \times 2}$ is a labeling vector indicating voxel foreground (background) probabilities. In our nasal cavity segmentation problem, we define a new energy term which holds the captured shape variances from the nasal SSM to the labeling vector of image voxels. The labeling vector can be optimized by solving a graph Dirichlet problem to produce the final probabilistic labeling. The proposed energy term was defined as:

$$E_{priors} = (z - (U_k\alpha + \bar{x}_{prob}))^{\mathrm{T}}(z - (U_k\alpha + \bar{x}_{prob})) \quad (1)$$

where $\bar{x}_{prob} = \frac{1}{1+\exp(\bar{x})}$ and $z = \begin{bmatrix} z_M \\ z_N \end{bmatrix}$, where z_M denotes the predefined labels i.e. foreground and background seeds, and z_N denotes other labels. Given the definition of E_{priors}, the complete energy function is formulated as $E_{total} = E_{rw} + E_{priors}$.

An estimation of the nasal cavity is obtained by minimizing the proposed functional $E_{total}(z_N, \alpha)$, iteratively, with respect to each of its variables z_N and α. First, we start from the mean shape and initialize $\alpha = 0$. Since E_{total} is convex, we differentiate E_{total} with respect to z_N and find the critical point yielding:

$$z_N = (L_N + I)^{-1}(2(U_k\alpha + \bar{x}_{prob}) - B^{\mathrm{T}} z_M) \quad (2)$$

where I is an identity matrix, L is the Laplacian matrix of the image and B is the matrix partitioned from L which correlates the labeled set to the unlabeled set. Secondly, we use the updated z_N to differentiate E_{total} once more with respect to α, which yields the following:

$$\alpha = (U_k^{\mathrm{T}} U_k)^{-1} U_k^{\mathrm{T}} (z_N - \bar{x}). \quad (3)$$

In order to reduce the amount of over-segmentation caused by the influence of the shape prior term without lessening its effect, we constrained the output of E_{total} to remain within the boundaries of the nasal airway by computing a probability of the estimated foreground voxels and removing those that overlapped into the tissue regions based on their intensity value at each step of the differential iteration.

3. RESULTS

3.1 Experimental Setup

We performed the leave-one-out cross validation on 20 CT images (20 folds) where 19 ground truth labels were used each time for the creation of the PA and SSM. We set the initialization parameter $\sigma = 5$. This value was empirically derived based on experiment validations. We further evaluated the effects of our proposed local constraint (LC) on nasal segmentation by running our algorithm with and without it.

We compared our algorithm to both the conventional and recent state-of-the-art segmentation algorithms including Probabilistic Multi Atlas (MA) [22], Grow-Cut (GC) [23], Seeded Region Growing (SRG) [24], Random Walker (RW) [18], Distance Regularized Level Set (DRLSE) [25], and Laplacian Coordinates (LAP) [26]. For MA, consistent to our algorithm, for each test images, 19 atlases were registered into the input image and the final result was the average of the transformed labels. We used the same seeds derived from our algorithm to initialize the segmentation for GC, SRG, LAP, DRLSE and RW.

We used the following metrics for the evaluation of segmentation results: (i) dice similarity coefficient (DSC) calculated as the overlap between the two volumes according to: $DSC = \frac{2\,|X \cap Y|}{|X|+|Y|}$ where X is the segmentation label and Y is the ground truth label; (ii) average symmetric surface distance (ASSD in mm); (iii) average symmetric root mean square surface distance (ASRSD in mm); (iv) maximum surface distance (MSD in mm); and (v) volumetric overlap error (VOE in %). Further details on the evaluation metrics may be found in Heimann et al. [27].

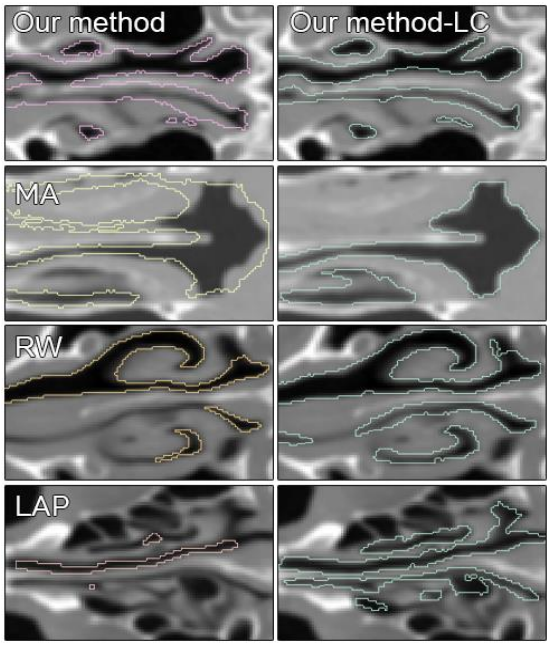

Figure 2. Comparison of our method with the LC (right column) against our method without LC, MA, RW, and LAP

3.2 Experimental Results

Table 1 presents the segmentation results of our algorithm compared to other methods. Our algorithm with the local constraint (LC) achieved the highest averaged DSC (89%), the lowest averaged distance error (0.29 *mm*), the lowest ASRSD (0.82 *mm*), the lowest MSD (6.74 *mm*), and the least amount of VOE (19.8%).

Evaluation Metrics	*DSC*	*ASSD*	*ASRSD*	*MSD*	*VOE*
Our method-LC	**89.0**	**0.29**	**0.82**	**6.74**	**19.8**
Our method	80.8	0.43	0.96	6.82	32.1
MA	75.2	0.48	0.83	6.83	39.5
RW	61.3	0.98	1.57	8.82	55.0
LAP	60.6	1.11	1.77	9.48	55.8
DRLSE	54.0	1.69	2.61	11.9	62.5
GC	31.2	1.47	2.57	20.2	53.8
SRG	30.5	1.02	1.78	12.7	59.1

Table 1. Comparative evaluation of our algorithm (with and without LC) and other methods at segmenting the nasal cavity

Quantitative evaluation of our proposed algorithm both with (blue) and without LC (orange) when compared against RW (gray) is shown in figure 3 below. We selected RW as the method for comparison to demonstrate the effect of the SSM shape priors on nasal segmentation. Our algorithm which incorporated LC achieved the best minimum (83.6%) and maximum (93.5%).

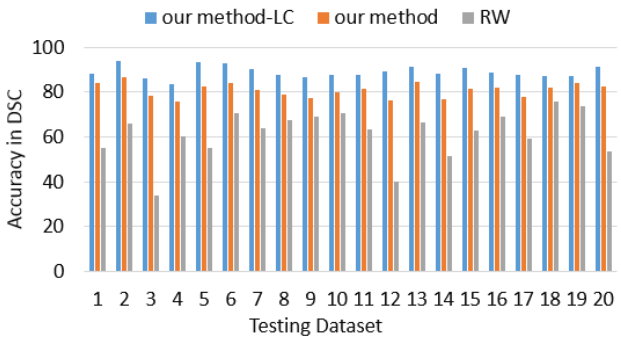

Figure 3. A quantitative DSC evaluation of our algorithm with the effect of LC compared to without LC and RW on a cohort of 20 nasal CT volumes.

4. DISCUSSION

Our algorithm had the best overall performance while the majority of the compared methods underperformed considerably. This was mainly attributed to the extreme narrowness and the wide range of voxel intensity difference observed from many of the nasal passages. Figure 2 illustrated where the majority of the segmentation errors occur at for other algorithms. Region-based methods (RW, LAP, GC, SRG) all experienced the same weakness at segmenting the narrower passages within the nasal cavity structure, mainly caused by the fuzziness of the voxel intensity. RW, LAP, and DRLSE performed considerably better than GC and SRG due to the advantage of the background seeds which prevented the majority of the leakage. GC and SRG suffered from both under-segmentation and over-segmentation, with the majority of the over-segmented area being at the entrance of the nostrils. Algorithms that made use of prior knowledge (MA and our methods) performed better in our experiments due to their ability to detect the narrower airway passages within the nasal structure. Both the MA and our method which did not make use of the LC suffered more from over-segmentation as shown in figure 2. The effect of our proposed LC greatly reduced the amount of over-segmentation.

5. CONCLUSION

We proposed an algorithm to automatically segment the nasal cavity, and thus, separating it from its surrounding structures in the upper respiratory tract. We then demonstrated its superior performance when compared to other well-known segmentation methods.

6. REFERENCES

[1] J. Cisonni, *et al.*, "Numerical simulation of pharyngeal airflow applied to obstructive sleep apnea: effect of the nasal cavity in anatomically accurate airway models," *Med Biol Eng Comput*, 1-11, 2015.

[2] N. Alsufyani, *et al.*, "Three-dimensional segmentation of the upper airway using cone beam CT: a systematic review," *Dentomaxillofacial Radiology*, 2014.

[3] J. S. Rhee, "Measuring outcomes in nasal surgery: realities and possibilities," *Arch Facial plastic S*, 11:416-419, 2009.

[4] K. Inthavong, *et al.*, "Simulation of sprayed particle deposition in a human nasal cavity including a nasal spray device," *Journal of Aerosol S*, 42:100-13, 2011.

[5] H. Shi, *et al.*, "Laminar airflow and nanoparticle or vapor deposition in a human nasal cavity model," *J Biomed Eng*, 128:697-706, 2006.

[6] K. Tingelhoff, *et al.*, "Comparison between manual and semi-automatic segmentation of nasal cavity and paranasal sinuses from CT images", Proc. *EMBS*, pp. 5505-8, 2007.

[7] A. Seo, *et al.*, "Semiautomatic segmentation of nasal airway based on collaborative environment," *ISUVR*, 2010, pp. 56-59.

[8] P. Dastidar, *et al.*, "Semi-automatic segmentation of computed tomographic images in volumetric estimation of nasal airway," *European Arch Oto-rhino-laryngology*, 256:192-8, 1999.

[9] H. Shi, *et al.*, "Upper airway segmentation and dimensions estimation from cone-beam CT image datasets," *Int J Comp Astd Radiol Surg*, 1:177-86, 2006.

[10] T. Iwasaki, *et al.*, "Evaluation of upper airway obstruction in Class II children with fluid-mechanical simulation," *Am J Orthod dentofac*, 139:e135-e145, 2011.

[11] A. S. El, *et al.*, "A 3-dimensional airway analysis of an obstructive sleep apnea surgical correction with cone beam computed tomography," *J Oral Maxil Surg*, 69:2424-2436, 2011.

[12] N. L. Bui, *et al.*, "Automatic segmentation of the nasal cavity and paranasal sinuses from cone-beam CT images," *Int J Comp Astd Radiol Surg*, pp. 1-9, 2014.

[13] C. Last, *et al.*, "A model-based approach to the segmentation of nasal cavity and paranasal sinus boundaries," in *Pattern Recogn*, ed: Springer, 2010, pp. 333-342.

[14] Kim, Sung Kyun, et al. "Patient specific CFD models of nasal airflow: overview of methods and challenges." Journal of biomechanics 46.2 (2013): 299-306.

[15] N. Morgan, *et al.*, "Racial differences in nasal fossa dimensions determined by acoustic rhinometry," *Rhinology*, 33:224-228, 1995.

[16] T. Heimann, *et al.*, "Statistical shape models for 3D medical image segmentation: A review," *Med Image Anal*, 13:543-63, 2009.

[17] M. E. Leventon, *et al.*, "Statistical shape influence in geodesic active contours," in *CVPR, 2000*, pp. 316-323.

[18] L. Grady, "Random walks for image segmentation," *IEEE T Pattern Anal*, 28: 1768-1783, 2006.

[19] S. Tomoshige, *et al.*, "A conditional statistical shape model with integrated error estimation of the conditions; Application to liver segmentation in non-contrast CT images," *Med Image Anal*, 18:130-143, 2014.

[20] A. Criminisi, *et al.*, "Geos: Geodesic image segmentation," *Lect Notes Comput SC*, ed: Springer, 2008, pp. 99-112.

[21] S. Klein, *et al.*, "Elastix: a toolbox for intensity-based medical image registration," *Medical Imaging, IEEE Transactions on*, vol. 29, pp. 196-205, 2010.

[22] E. van Rikxoort, *et al.*, "Automatic segmentation of the liver in computed tomography scans with voxel classification and atlas matching", *MICCAI segmentation workshop*, pp. 101-8, 2007.

[23] V. Vladimir, *et al.*, "GrowCut: Interactive multi-label ND image segmentation by cellular automata." proc. of Graphicon. 2005.

[24] E. Day, *et al.*, "A region growing method for tumor volume segmentation on PET images for rectal and anal cancer patients," *Med physics*, vol. 36, pp. 4349-4358, 2009.

[25] C. Li, *et al.*, "Distance regularized level set evolution and its application to image segmentation," *Image Processing, IEEE Transactions on*, vol. 19, pp. 3243-3254, 2010.

[26] W. Casaca, *et al.*, "Laplacian Coordinates for Seeded Image Segmentation," *CVPR, 2014*, pp. 384-391.

[27] T. Heimann, *et al.*, "Comparison and evaluation of methods for liver segmentation from CT datasets," *Medical Imaging, IEEE Transactions on*, vol. 28, pp. 1251-1265, 2009.